Editors' Suggestion

Chiral Waveguides for Robust Waveguiding at the Deep Subwavelength Scale

B. Orazbayev, N. Kaina, and R. Fleury*

Laboratory of Wave Engineering, École Polytechnique Fédérale de Lausanne (EPFL), 1015 Lausanne, Switzerland

(Received 27 August 2018; revised manuscript received 31 October 2018; published 30 November 2018)

Routing electromagnetic energy at a scale smaller than the wavelength is a highly sought functionality in a variety of applications, including compact lightweight satellite communications, slow-waves sensors, all-optical information processing, and energy harvesting. Unfortunately, strong field confinement at this scale requires the use of coupled subwavelength resonators, implying a large sensitivity to geometrical imperfections and disorder-induced backscattering. We propose a very unconventional solution to this problem by exploiting the interface modes occurring at the boundary between two chiral metamaterials composed of resonant metamolecules with opposite chirality. Our numerical and experimental results demonstrate the inherent robustness of these interface states to disorder in both the position and resonance frequency of the metamaterial's meta-atoms. By computing transmission averages over many realizations of disorder, we quantitatively demonstrate the superiority of this form of subwavelength routing over previously proposed designs, including frequency-defect lines, symmetry-based topological edge modes, and Valley-Hall interface states.

DOI: 10.1103/PhysRevApplied.10.054069

I. INTRODUCTION

For centuries, the ability to guide and process electromagnetic signals and energy has been one of the most important scientific and technological challenges. Wave routing is commonly achieved using standard metallic or dielectric waveguides, whose overall dimensions are fundamentally tied to the wavelength of operation. Basic signal-processing tasks, like filtering and duplexing, also typically involve a wavelength-scaled structure that exploits Bragg interferences [1]. The incompressible size of these key wave devices is a particularly vexing issue at microwave frequencies, where the wavelength can be of the order of tens of centimeters, resulting in heavy and bulky communication devices. Reducing the cost associated with sending these large and heavy metallic structures to space is a crucial challenge in the development of cost-efficient satellite communications. In a different application field, the quest for all-optical information processing is also driving a considerable research effort for developing small and robust optical interconnects with high transmission rates and high-speed data-processing capabilities [2].

On the other hand, the recent development of metamaterials, artificial media based on the complex interaction between an external wave and an ensemble of resonant inclusions, has provided a new tool to efficiently manipulate waves down to the deep subwavelength regime [3,4]. For instance, devices based on so-called locally resonant metamaterials, such as waveguides and filters [5], make possible the manipulation of electromagnetic energy well below the diffraction limit [6]. One good example is a subwavelength waveguide formed by inserting a frequency-defect line of resonators into a locally resonant metamaterial [6,7]. In such a medium, the resonant meta-atoms constituting the metamaterial interact with propagating plane waves, through both multiple scattering and a Fano interference effect, leading to propagation properties exhibiting a band gap above the meta-atom resonance frequency [8,9] that mainly stems from the meta-atom resonance property. Therefore, analogous to defect cavities in photonic crystals, it is possible to confine and guide waves inside the medium by inserting a line of defect resonators. However, contrary to Bragg interference-based media [10], whose properties depend on the material wavelength-scaled structure, the typical defect in metamaterials is achieved by modifying the resonance frequency of one or several subwavelength meta-atoms so that it falls into the band gap of the surrounding medium, hence allowing deeply subwavelength wave confinements. Moreover, since the band gap of the locally resonant metamaterials relies on the resonant nature of the particles rather than on their spatial arrangement (i.e., periodical structure), the wave propagation is less sensitive to the structural deformations of the defect line. This provides a

*romain.fleury@epfl.ch

certain degree of robustness of the waveguide to spatial disorder [7], an important issue in photonic crystal-based waveguides [11,12]. Nevertheless, since the defect resonance plays a major role in the waveguiding mechanism, we might expect the latter to be less robust against disorder that would affect the defect-line resonance frequency, similar to coupled-resonators optical waveguides [13,14].

To tackle the problem of robustness of photonic crystal-based waveguides against disorder, more advanced designs based on topological concepts have been suggested to confer some form of topological protection to these wavelength-scaled devices [15–22], including time-reversal (TR) symmetric photonic-topological insulators based on six-fold rotational lattice symmetry (C_{6v}) [23] or Valley spins [24]. Derived from the solid-state approach, the topological protection in these designs naturally relies on the structural composition of the media. Despite the deep subwavelength nature of locally resonant metamaterials, it was recently demonstrated that spatial structuration, through multiple scattering phenomena, also plays a crucial role at this scale, determining the wave propagation properties in such media [6,9], hence allowing the transposition of some form of topological protection to the deeply subwavelength scale [25]. Unfortunately, since in all time-reversal invariant designs the topological properties mostly stem from the complex crystalline nature and frequency dispersion of the metamaterial, most of disorders, be it in the position or in the frequency of the constitutive meta-atoms, may strongly break the lattice symmetries and couple together time-reversed modes. Therefore, the efficiency of these topological designs in terms of robustness to defects and fabrication uncertainties has yet to be rigorously studied.

Here, we propose and experimentally demonstrate an alternative solution to guide electromagnetic waves at the subwavelength scale that is neither based on frequency-defect tunneling, spatial structuration, nor topological bulk properties, but rather on a much sturdier property: chirality [26–28]. While performing ensemble averages on disorder realizations along the path of the guided wave, we rigorously and quantitatively demonstrate its superior robustness to the introduction of either spatial or frequency disorders, over previously proposed subwavelength-guiding designs, namely frequency-defect lines, symmetry-based topological edge modes, and valley-interface states. We present both numerical and experimental results in the microwave regime, although the concept remains very general and can be applied to other frequency ranges or types of waves.

II. RESULTS

A. Design of a chiral metamaterial

We start by considering the elementary building block (metamolecule) of the chiral metamaterial. It consists of four quarter-wavelength resonant metallic wires standing on a ground plane [29]. These metallic rods have different lengths, leading to distinct individual resonance frequencies distributed around a central frequency f_c ($f_{1,4} = f_c \mp 2\Delta, f_{2,3} = f_c \mp \Delta, \Delta = 0.05 f_c$), as shown in Fig. 1(a). The wires are arranged on a deep subwavelength square of side $c = 0.02\lambda_c$ (λ_c is a wavelength at f_c) and can be distributed clockwise (CW) or counterclockwise (CCW) with growing frequencies in a square lattice of period $a = 2c$, also deeply subwavelength. Depending on the direction of the rotation, the metamolecule can then exhibit two opposed chiralities [26–28]. Using a semi-analytical model based on coupled dipoles [25,30,31], we obtain the four individual modes of both CW and CCW elementary metamolecules [see Fig. 1(a)], resonating at frequencies close to f_{1-4}. From the electric-field distribution [right panel of Fig. 1(a)], we see that each of these resonant modes corresponds to the harmonic oscillations of one specific resonator of the metamolecule. From Fig. 1(b), we furthermore observe that the CW and CCW metamolecules obviously support resonant modes at the same frequencies, but with opposite chirality of field-distribution symmetry.

From these elementary metamolecules, we can move now to the bulk medium, i.e., two-dimensional (2D) lattice [see Fig. 1(c)]. The previously discrete resonant modes of the elementary unit cell now result in a dispersion relation composed of successions of propagative bands separated by band gaps (the three green-shaded regions), each of the bands lying below one of the resonant frequencies f_{1-4} of the individual molecule [blue lines in right panel of Figs. 1(a) and 1(b)]. Note that both types of bulk media, made of CW or CCW elementary metamolecules, present the exact same dispersion relation. This is naturally expected since the single metamolecules eigenfrequencies are identical. Another intuitive explanation lies in the fact that each bulk medium can be equivalently described by one or the other elementary metamolecules simply by shifting the unit cell by half a period, which, of course, should not affect the bulk properties of the infinite chain. Although trivial, this property is crucial for the existence of localized edge modes at the interface between two metamaterials with opposite chirality.

B. Chirality-induced edge modes

Next, we investigate the existence of localized modes at the interface between two linear chains composed of metamolecules with opposite chirality by first analyzing the resonant eigenmodes that are supported by the CW-CCW compound formed by the two adjacent unit cells at the interface [top panel of Fig. 2(a)]. Since this supermetamolecule (composed of eight resonators) contains a newly formed nonchiral defect metamolecule exactly at the interface [the four center resonators circled with a black dashed line in the top panel of Fig. 2(a)], it is expected

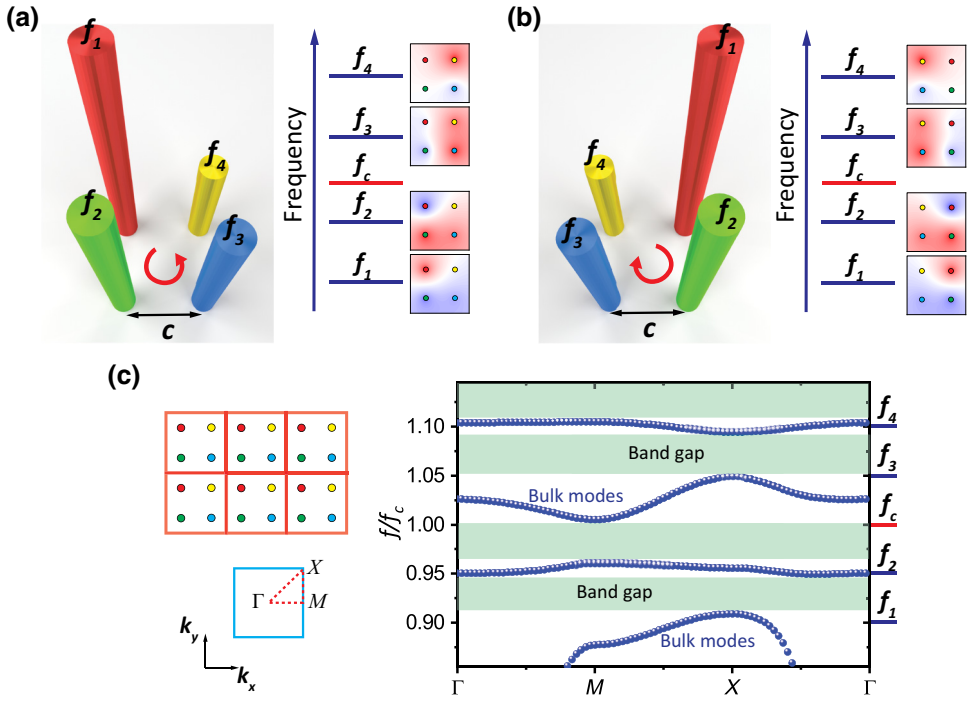

FIG. 1. Interface states based on metamaterials with opposite chirality. (a) Chiral metamolecule composed of 4 quarter-wavelength conducting posts with different resonance frequencies ($f_{1,4} = f_c \mp 2\Delta, f_{2,3} = f_c \mp \Delta, \Delta = 0.05 f_c$) distributed CCW on a ground plane. Its modes are shown in the right panel along with their resonant frequencies (solid blue lines). (b) Metamolecule built from the same posts as in (a), but distributed CW. (c) Numerical band structure of a bulk crystal made from the chiral metamolecule. The bulk modes are followed by complete band gaps (green-shaded regions).

to support additional eigenmodes on top of the initial CW and CCW metamolecules' eigenmodes. We focus on these new modes, with resonance frequencies f_{e1-e4}. As shown by the calculated field distributions at these defect frequencies [bottom right panel of Fig. 2(a)], the lowest energy mode (f_{e1}) in the second band gap is of monopolar symmetry with all resonators oscillating in phase, while higher energy modes (f_{e2-e4}) are antisymmetric. We furthermore observe, from extended simulations of the electric-field distribution in a composite one-dimensional (1D) chain of five CW and five CCW metamolecules [Fig. 2(b) for the first mode f_{e1}], that these modes are spatially confined inside the defect metamolecule at the interface. This attests that they are spectrally localized in the surrounding chains' band gap regions, making them good candidates as elementary unit cells to create subwavelength waveguides in an extended 2D medium.

Prior to exploring the properties of such potential waveguides, we first focus only on the single-interface super-metamolecule of the previous linear chain to see how it is affected by either spatial or spectral disorder [see top panel of Fig. 2(c)]. The robustness of the waveguide that will be created from this linear interface is indeed foreseen by the ability of the induced disorder to modify or not the considered interface-mode symmetry. To this end, we focus on the first mode f_{e1}, which is expected to be less sensitive to disorder given its monopolar nature. We then calculate the field distribution at f_{e1} while introducing either position or frequency disorders in the interface, starting with the influence of positional disorder. The latter is introduced by displacing each of the four resonators within the interface-defect metamolecule by a distance R_{def} randomly chosen in the range $R_{\text{def}} = [0, c/2]$ and in an arbitrarily chosen direction in the xOy plane. The electric-field distribution in this deformed interface for one specific realization of spatial disorder [Fig. 2(c), central panel] demonstrates that even such a significant displacement of the resonators (up to half the unit cell size) does not break the chirality of the interface adjacent CW and CCW metamolecules while preserving the f_{e1} edge-mode symmetry. This suggests a strong robustness of the system regarding positioning disorder. Let us now move to the second kind of disorder that can be induced and demonstrate that this edge mode is also, to some extent, robust to frequency modifications of the single-rod resonances in the interface region. To do so, we apply the same frequency-disorder strength δf to each of the four resonators of the defect metamolecule [circled with a dashed line in Fig. 2(c)]. Several cases then have to be considered depending on the disorder strength δf. If the frequency disorder is kept small enough compared to the resonance-frequency modulation Δ (i.e., $|\delta f| \leq \Delta$), the symmetry of the f_{e1}-edge

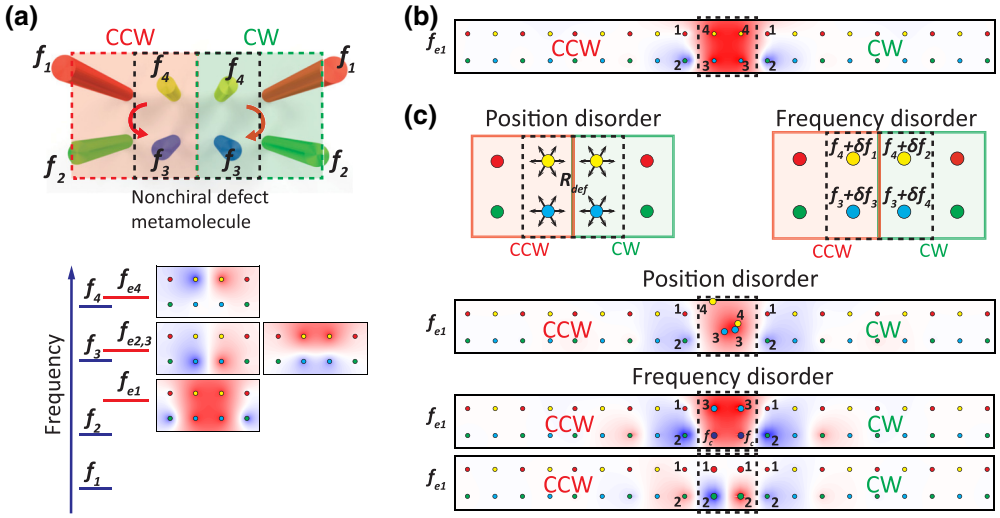

FIG. 2. Localized edge modes at the interface between two linear chains of opposite chirality. (a) Creation of a defect metamolecule with no intrinsic chirality (circled with dashed lines) and with additional resonant states induced at the interface (bottom inset). The resonance frequencies f_{e1-e4} of this defect metamolecule fall within the forbidden regions of the adjacent chiral linear chains. (b) First-edge-mode field distribution in a 1D chain of 5 CW and 5 CCW metamolecules. (c) The presence of this interface state is strongly robust to random position (middle panel) and frequency disorders (bottom panels) that do not change the chirality on both sides of the interface.

mode remains intact, suggesting its robustness to small frequency disorders. This can be observed, for instance, in the limit case, where $\delta f = -\Delta$ is applied to resonators $f_{3,4}$ converting them into resonators with frequencies f_c,f_3, respectively [third panel in Fig. 3(c)]. Nevertheless, when the interface is modulated by frequency shifts $|\delta f| > 2\Delta$, a modulation large enough to change the chirality of both the CW- and CCW-adjacent interface unit cells and the defect metamolecule itself, the localized mode f_{e1}, is generally either destroyed (not localized at the interface) or of altered mode symmetry (to a dipolar one, for instance). This is highlighted in Fig. 2(c) (bottom panel), where a frequency shift $\delta f = -2\Delta$ is applied to resonators f_{3-4}, converting them into resonators f_{1-2}. The corresponding field distribution confirms a complete destruction of a monopolar mode f_{e1} and its replacement with a dipolar mode that has a field structure close to the mode f_{e2}.

C. Robust wave transport in a chiral waveguide

We finally move to the 2D case by repeating the linear 1D chain of the CW-CCW metamolecules along the perpendicular direction to allow this localized edge state to propagate, effectively forming a waveguide at the interface [see Fig. 3(a)]. The numerical band structures [31] obtained for the 8×1 supercell containing unit cells of one chiral medium (blue spheres) and the interface between the media with opposite chirality (red spheres) demonstrate the appearance of several additional bands localized at the interface, and therefore, confirm our semi-analytical results, as shown in Fig. 3(b).

Nevertheless, from now on, we will focus on the band in the second band gap (with a bandwidth B_{CH}) that corresponds to the even edge modes with monopolar field distribution (f_{e1}). To investigate the propagation of the edge defect modes at the interface, we exploit the previously described semi-analytical model, but we now introduce an external source to excite the structure from one side of the crystal. The transmission is captured at the opposite anechoic end [31]. The electric field distribution for a frequency chosen in this band [see Fig. 3(c)] effectively demonstrates a propagating localized edge mode in the interface between two media with opposite chirality, confirming the formation of a waveguide based on the chiral metamaterial. Due to the subwavelength structuration of the metamaterial, this propagation occurs with a subwavelength-transverse confinement of width $W_{CH} \approx 0.03\lambda_c$, the order of the interface defect metamolecule dimension. The point is now to demonstrate the robustness of this guided mode in the presence of disorder. To that aim, we first introduce a random positioning disorder at a given location along the propagation path at the interface. We apply it to all interface resonators enclosed in the square box of size W_{CH}, so that the position disorder affects the region where most of the energy flux is localized. The electric-field distribution is then first calculated for a spatial disorder, as the resonators enclosed in the box are randomly shifted in the range $R_{def} = [0, 0.1W_{CH}]$. The calculated 2D color map of the normalized electric-field distribution for one specific disorder realization is shown in Fig. 3(d) (affected resonators are plotted with red dots). Next, the electric-field distribution is also calculated

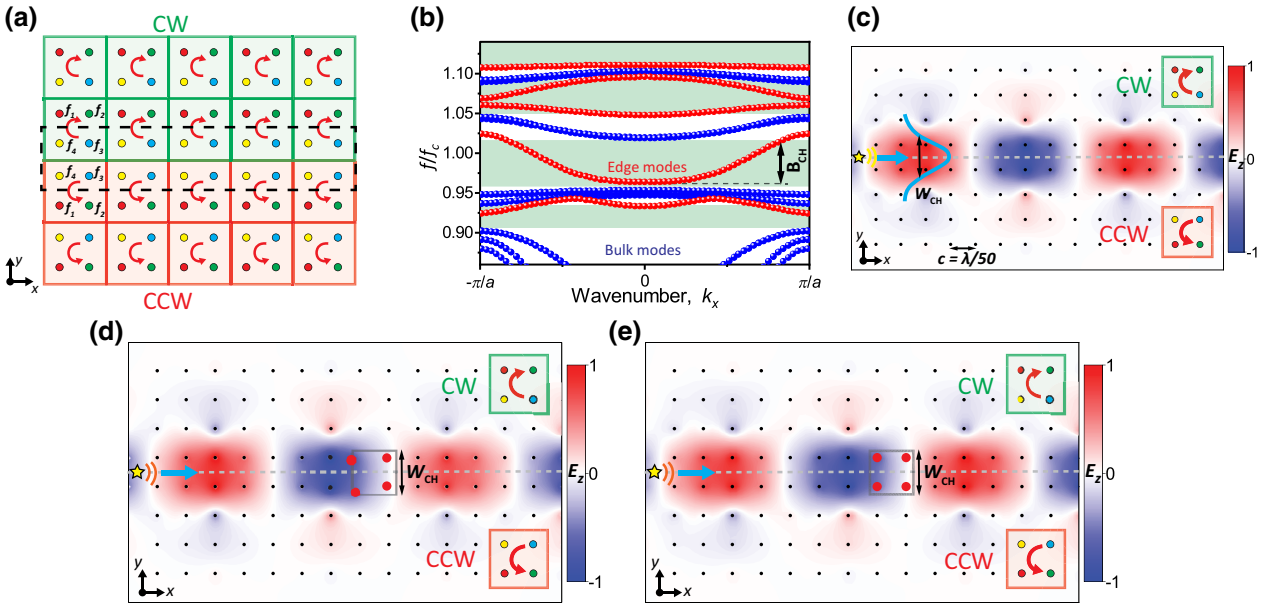

FIG. 3. Robust subwavelength transport in a chiral waveguide. (a) The linear chain of Fig. 1(b) is periodically extended along the x direction to allow wave guiding along the interface (dashed line). (b) The numerical band structure of an 8×1 supercell with uniform chirality (blue spheres), compared to the one of the same supercell containing a chirality switch creating an interface at the center (red spheres). (c) Field distribution of the first monopolar edge mode (f_{e1}) along the interface between two chiral media with different handedness. (d) Field distribution for the first monopolar edge mode (f_{e1}) in the presence of spatial disorder (with a displacement R_{def} in the range $[0, 0.1W_{\text{CH}}]$). (e) Field distribution for the first monopolar edge mode (f_{e1}) in the presence of frequency disorder (with a disorder strength δf in the range $[0, 1.22\text{B}_{\text{CH}}]$).

for a realization of frequency disorder, as the resonance frequencies of resonators enclosed in the box are randomly shifted in the range $\delta f = [0, 1.22\text{B}_{\text{CH}}]$ [Fig. 2(e)]. From the figures, it is clear that despite the significant displacement of the resonators or changes in their resonance frequencies, the propagation is practically unaffected (although with small, albeit noticeable, backscattering), suggesting the potential robustness of the chiral waveguide. The link between defect-protection and chirality is confirmed by direct calculations of its chirality in the absence and presence of defects of different strengths, $C_m = (\omega/2c^2)\text{Im}[\mathbf{E} \cdot \mathbf{H}^*]$, where bold letters are the complex field amplitudes [27,28,31]. However, such a claim of robustness must be quantitatively confirmed by performing a statistical analysis, which we present in the last part of this paper.

D. Experimental demonstration

Based on these theoretical results, we have built a sample of a robust chiral subwavelength waveguide as shown in Fig. 4(a). In such a sample, the resonators of the chiral medium are made of half-wavelength-resonant metallic stripes (with $f_c = 4.5$ GHz, $\Delta = 0.05f_c = 0.225$ GHz) by 2D printing them onto transparent foam sheets to form a freestanding square lattice with a period of $a = 12.7$ mm $= 0.19\lambda_c$ [31]. First, we explore the transmission through a bulk medium with uniform chirality using a vector network analyzer (VNA). To excite this structure, an antenna (Tx) is placed at one side of the sample while another short antenna, mounted in a 2D-moving stage, is used to scan the near-field distribution of the electric field all over the sample. The transmission spectrum of the bulk, displayed in Fig. 4(b) (dashed gray line), is obtained by averaging the amplitude over nine unit cells far away from the source. As predicted by the semi-analytical analysis, four band gaps [green-shaded areas in Fig. 3(a)] are observed. We then modify the chirality of half of the metamaterial and measure the new transmission spectrum [Fig. 4(b), solid red line]. We now observe that five transmission bands emerge in the band gaps of the surrounding bulks [marked with the numbers in Fig. 4(b)]. By looking at the 2D-field maps at the frequencies of these transmission bands, we find that they correspond to the excitation of the different edge modes at the interface between the media with different chirality, consistent with our semi-analytical results. Moreover, the experimental 2D-field map at the frequency within the second band [at $f_{\text{exp}} = 4.4$ GHz shown in Fig. 4(b)] confirms the existence of the monopolar edge modes and their subwavelength nature ($W_{\text{exp}} \approx 9.5$ mm $\approx 0.14\lambda_{\text{exp}}$), perfectly matching the previously obtained semi-analytical 2D-field map. Note that the transmission for the edge mode bands exceeds the transmission in the bulk, which is due to the

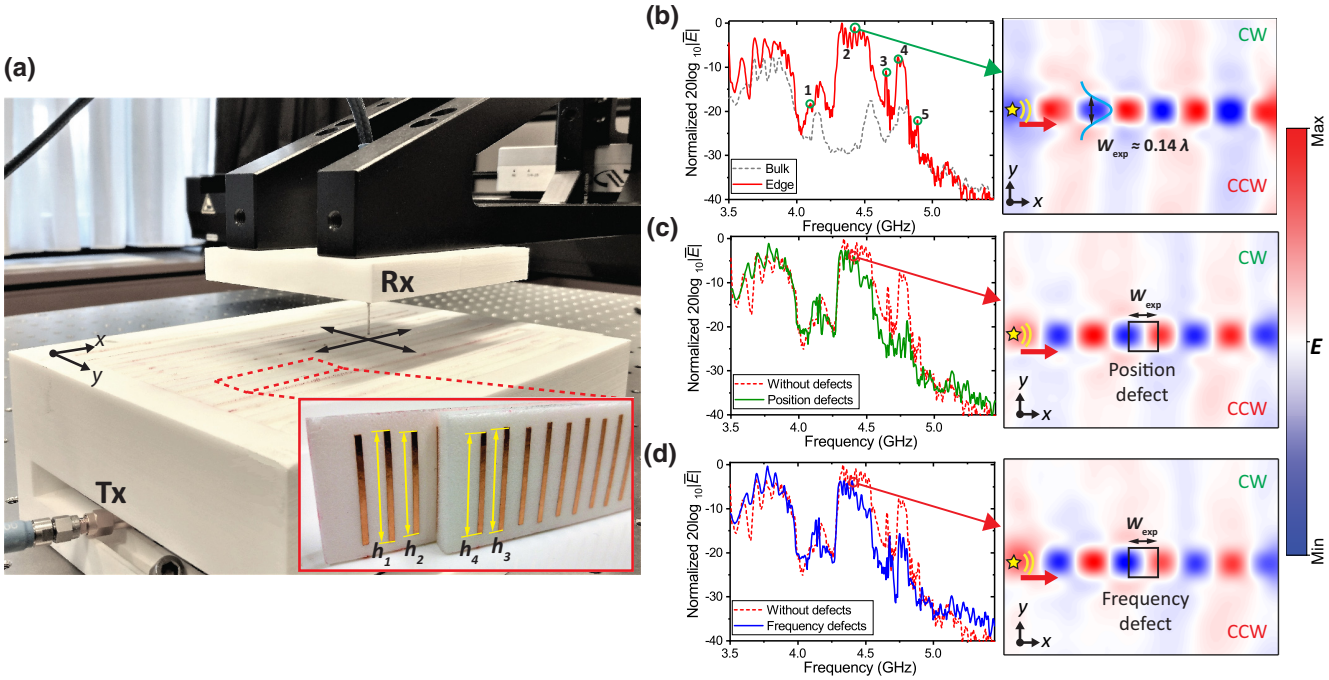

FIG. 4. Experimental validation of the robustness of subwavelength chiral waveguides. (a) Photograph of the experimental setup allowing for scanning the near field above the sample. In panel, detailed view of the fabricated half-wavelength copper dipoles composing the chiral metamaterial. The transmitter (Tx) and receiver (Rx) are connected to a VNA. Rx is placed on a 2D translational stage and allows capturing the full 2D-field distribution. (b–d) Experimental transmission spectra and measured field maps for (b) the chiral interface without disorder, (c) the interface with position disorder of strength $R_{\mathrm{def}} = 0.1W_{\mathrm{exp}}$, and (d) with frequency disorder of strength $\delta f = 1.22\mathrm{B}$.

confinement of the energy on the interface, contrary to the uniformly spread bulk modes. It should be noted that the field confinement of the edge modes in the z axis is due to the subwavelength nature of these modes, which prevents the out-of-plane leakage of the surface wave.

We finally experimentally demonstrate the electromagnetic propagation robustness in the chiral-metamaterial waveguide while considering two realizations of disorder (spatial and spectral) along the waveguide. This is done by changing the position or resonance frequency of four resonators enclosed in a square box of size W_{exp} along the interface [see Figs. 4(c) and 4(d)]. The maximum experimental disorder strength is set to $R_{\mathrm{def}} = 0.1W_{\mathrm{exp}}(0.95\ \mathrm{mm})$ and $\delta f = 1.22\mathrm{B}_{\mathrm{exp}}(0.22\ \mathrm{GHz})$ for position and frequency disorders, respectively. The measured transmission spectra for both position and frequency disorders are shown in Figs. 4(c) and 4(d) (left panels), respectively, showing that the edge modes of the second band propagate almost without scattering loss along the interface. The corresponding experimental 2D-electric-field maps for this band [Figs. 4(c) and 4(d), right panels] demonstrate a mostly uniform amplitude along the interface, hence confirming the absence of strong backscattering. Altogether, the experimental results agree very well with the results obtained in the theoretical analysis and validate the strong robustness of the monopolar mode of the chiral waveguide to spatial and frequency disorder. Note that, as is predicted by our semi-analytical results, bands based on higher-symmetry interface modes are more sensitive to disorder resulting in a higher transmission drop. Moreover, it should be noted that another type of backscattering source, a bent-waveguide interface, can be considered, and it can also reduce the overall performance of the waveguide [31].

Now, to quantitatively demonstrate the superior robustness of the chiral subwavelength-guiding scheme, we finally compare it to three other subwavelength-guiding schemes shown in Fig. 5. These designs are all based on locally resonant metamaterials and have previously demonstrated a certain degree of protection of the propagating edge modes, namely (a) a frequency-defect line waveguide [6,7] (b) a C_{6v}-symmetry-protected quantum-spin Hall (QSP) photonic-topological insulator (PTI) [23,25], and (c) a quantum Valley-Hall (QVH) PTI [24,31].

E. Statistical analysis of the robustness of different waveguide systems

To this end, we perform a statistical analysis on all waveguide systems by evaluating the transmission

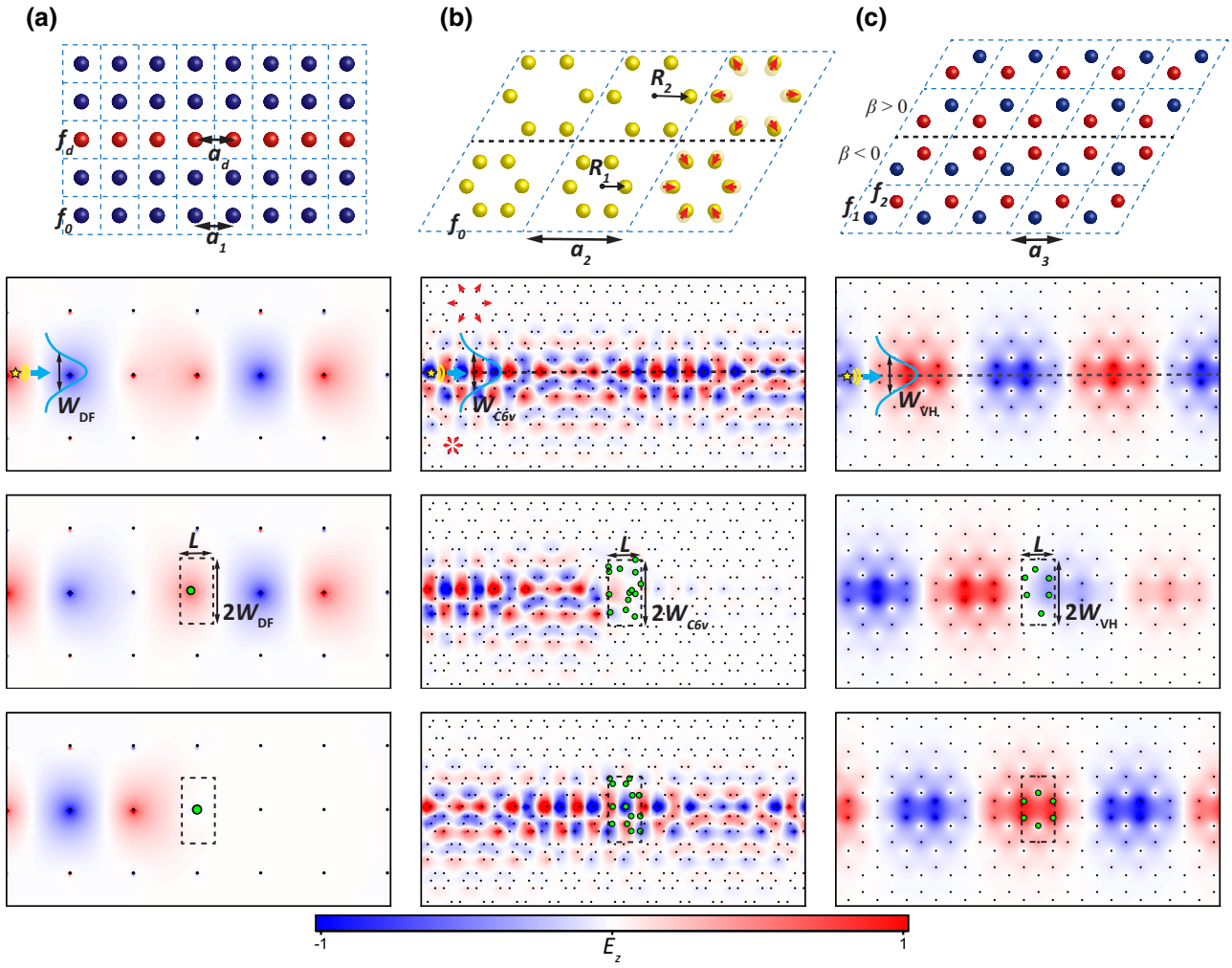

FIG. 5. Other solutions to achieve subwavelength waveguiding based on locally resonant metamaterials. To quantitatively prove the superior robustness of the chiral waveguide, we compare it with three alternatives that provide guided modes (second row panels) with an identical group velocity as our chiral-guided state. We expose them to position (third row panels) and frequency (fourth row panels) disorders contained in a box of size $2W \times L$ along the interface, where W is the transverse mode width and L is the varying box length. Each post within this box is affected by a random disorder in the range $[0, 0.2W]$ for position and $[-\mathrm{B}, \mathrm{B}]$ for frequency disorders (BW is the bandwidth of the transmission band for each waveguide). (a) Defect mode propagating along the frequency-defect line (second panel) with a mode width W_{DF} . (b) Edge mode propagating along the armchair interface of C_{6v}-symmetry waveguide (second panel) with a mode width W_{C6v}. (c) Edge mode propagating along the interface of Valley-Hall waveguide (second panel) with a transverse mode width W_{VH} .

coefficient (S_{21}) while introducing both kind of disorders with varying disorder strength [31]. For the sake of simplicity, in the analysis, we focus on a single-frequency operation, at which each of the compared waveguides provides its best performance [31]. Moreover, to have a systematic comparison of waveguide performances despite the different geometries, we define a consistent methodology in which the group velocities at the chosen frequencies are equal for each type of waveguide [31]. Furthermore, to be sure that the created disorder will similarly challenge the propagation in each of the compared waveguides, the width of a rectangular box in which the disorder will be applied is set to be equal to two transverse widths of the propagating edge mode in each waveguide [see Figs. 5(a)–5(c)]. Hence, different guiding systems can be fairly compared without the need to scale them by defining the normalized strength of spatial disorder to be proportional to the transverse mode's width ($\tilde{R}_{\mathrm{def}} = R_{\mathrm{def}}/W_{\mathrm{CH,DF},C6v,\mathrm{VH}}$). The fair comparison for the case of frequency disorder is, on the other hand, implemented by normalizing the frequency-disorder strength by the transmission bandwidth of the considered propagating interface mode ($\delta\tilde{f} = \delta f / \mathrm{B}_{\mathrm{CH,DF},C6v,\mathrm{VH}}$). Note that since each waveguide has different unit cell geometry and

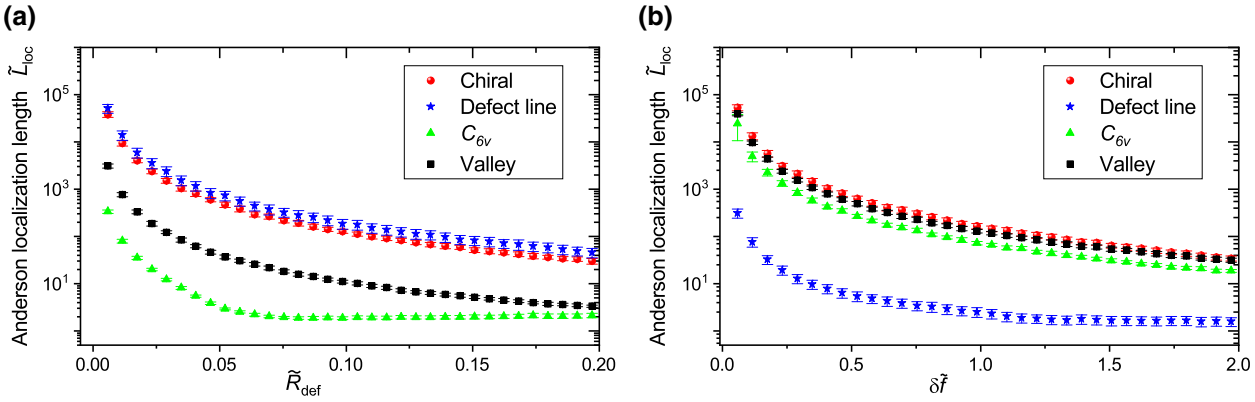

FIG. 6. Statistical analysis of robustness of four different subwavelength-guiding systems, demonstrating the superiority of the chiral design in the presence of disorder. Normalized Anderson localization length ($\tilde{L}_{loc} = L/W$) as a function of the amplitude of (a) position- ($\tilde{R}_{def}$) and (b) frequency- ($\delta\tilde{f}$) normalized disorders for the chiral (red circles), defect line (blue stars), C_{6v}-based (green triangles), and Valley-Hall- (black squares) based waveguides. Each point represents an inverse of the slope of the ensemble average logarithm of the numerically obtained transmission $\langle \ln S_{21} \rangle$ as a function of the disorder box length L. The vertical error bars represent the standard deviation of $\tilde{L}_{loc}$ for each disorder amplitude.

composition (six resonators in the C_{6v} waveguide, one only for the frequency-defect line), the disorder box can enclose a different number of resonators in each case.

One of the most important quantities in describing the wave propagation in a disordered system is the Anderson localization length, which measures the spatial decay of the localized states [32,33] and can be used to characterize the transport properties of the disordered medium or, in our case, the waveguide robustness. Therefore, we calculated the normalized Anderson localization lengths $\tilde{L}_{loc} = L/W_{CH,DF,C6v,VH}$ [31] as a function of the normalized disorder's strength. This was done for each guiding system [see Figs. 6(a) and 6(b)] and each type of disorder, to evaluate and compare their respective robustnesses. From Fig. 6(a), it can be observed that even for significant displacements of the resonators, the localization length in the chiral (red spheres) and defect line (blue stars) waveguides remains relatively high ($\tilde{L}_{loc} > 10^2$), which confirms their strong robustness to spatial disorder. On the contrary, equivalent spatial disorders in the C_{6v}-symmetry waveguide (green triangles) and Valley waveguide (black squares) result in a significant drop of $\tilde{L}_{loc}$, confirming their smaller robustness against such disorder. In the case of frequency disorders in the chiral waveguide system, the localization length is of the same order as for the position disorders, which proves its insensivity to disorder type [Fig. 6(b)]. This protection is comparable to the one obtained in the C_{6v}- and Valley-based waveguides that are less sensitive to resonance-frequency shifts along the waveguide. Contrary to these waveguides, we, however, observe that the localization length in the frequency-defect-line waveguide drops quickly even for the relatively small disorder strengths. Therefore, these results confirm the superior robustness of our chiral-metamaterial waveguide over other subwavelength waveguiding solutions, since it is the only solution that provides a strong protection against both types of disorder.

III. CONCLUDING REMARKS

The statistical analysis and experimental results presented here confirm the superior robustness of the chiral waveguide to both types of disorder, while other waveguide types compared in this work demonstrate a certain level of protection for either position or frequency disorder only [see Figs. 6(a) and 6(b)]. The general robustness of the chiral waveguide comes from the fact that the wave propagation is protected by the chirality of the adjacent media. For disorder to cause a significant level of backscattering, it is required to simultaneously break the polarization state of the monopolar edge mode and the chirality of the adjacent metamolecules. In the case of positional disorder, this imposes moving the resonators at distances comparable to the mode's transverse width. For frequency disorders, the strength is required to exceed the band separation $|\delta f| > \Delta$. Both of these conditions are barely limiting, since such disorder strengths are large enough to exceed typical spatial or frequency fabrication tolerances, which are the main source of disorder-induced backscattering in most linear waveguiding systems. This ensures large localization lengths or equivalently strong robustness of the propagation in the proposed waveguide.

As for the frequency-defect line waveguide, it is naturally robust to spatial displacements of the resonators, since the hybridization band gap is insensitive to the structural deformations of the medium [blue stars in Fig. 6(a)]. On the other hand, since the resonance frequency of particles is at the origin of the defect line creation, the wave

propagation is more sensitive to changes in the resonance frequency, making the wave propagation in this defect-line waveguide vulnerable to this type of disorder. In particular, even for frequency-disorder strengths smaller than the transmission bandwidth of the propagating defect mode, some backscattering is observed, and the localization length drops to several orders smaller than for the chiral waveguide [see Fig. 6(b)].

In the C_{6v}-symmetry waveguide, the polarization of the pseudospin states fully relies on the symmetry of the expanded and shrunk metamolecules. Therefore, for even small random displacements of the resonators ($R_{\mathrm{def}} \ll W_{C6v}$), the symmetry of metamolecules is locally broken, resulting in an intercoupling of the two pseudospin states. From this coupling originates backscattering of the propagating wave that reduces the localization length [green triangles in Fig. 6(a)], explaining the lower robustness of such waveguides to spatial disorders. Note that the armchair interface breaks the lattice symmetry by itself, which results in gapped and possibly less-robust edge states [23]. This gap can be reduced by introducing a zigzag interface or an adiabatic interface with gradually deformed hexagons, respectively [25,34]. However, both interfaces will result in less-localized edge waves, which also end up being affected by the lattice disorders, which take into account the fact that the modes are larger. On the other hand, the C_{6v}-symmetry waveguide is less sensitive to frequency disorder since it does not significantly change the symmetry of the expanded and shrunken metamolecules, providing a more robust waveguiding [see Fig. 6(b)].

Finally, the Valley-Hall waveguide, for which the topologically protected valley edge states originate from both spatial and frequency properties of the crystal, is logically sensitive to both position and frequency disorders. As expected, due to the reduced complexity of geometry compared to the C_{6v}-symmetry waveguide, the Valley waveguide demonstrates larger localization lengths for small disorder strengths that do not break the valley states of the crystal [black squares in Fig. 6(a)]. However, for disorders strong enough to break the lattice symmetry and mix the valley states [$R_{\mathrm{def}} \approx a_3$, a_3 is the unit cell period, see Fig. 5(c)], the robustness of the waveguide is equivalent to the C_{6v}-symmetry waveguide and the localization length inevitably converges to the minimum values of localization length ($\tilde{L}_{\mathrm{loc}} \approx W$). In the case of frequency disorder, breaking the valley states inside the metamolecules requires introducing disorder strengths exceeding the inversion-breaking frequency [$|\delta f| > \beta f_0$, where β is the symmetry-breaking parameter, f_0 is the central resonance frequency, see Fig. 5(c)]. Therefore, the valley states are also quite robust to frequency disorders, resulting in a localization length within the standard deviation of the ones observed in the chiral-metamaterial waveguide [see Fig. 6(b)].

In summary, we proposed and experimentally demonstrated in the microwave range a subwavelength-waveguiding system based on a locally resonant chiral metamaterial. By stacking two media with opposite chirality, a defect unit cell is created at the interface, which supports hybrid modes in the band gaps of both surrounding media, guaranteeing the existence of localized edge modes that propagate along the interface, forming subwavelength waveguides. We experimentally prove that these localized propagative modes are robust to both types of disorder that can be introduced in locally-resonant metamaterials, namely spatial and spectral disorders. The statistical study provides a complete assessment of the robustness to disorder of different types of waveguiding systems, including the systems based on frequency-defect line and PTIs with preserved TR symmetry. It has revealed that such systems, unlike the chiral waveguide, are robust only against either position or frequency disorder due to the nature of their localized edge modes. We emphasize that the chiral waveguide is free from such compromise and is promising for the practical realization of robust subwavelength-guiding systems, where it is crucial to obtain a high transmission despite the fabrication tolerances.

ACKNOWLEDGMENTS

N.K. acknowledges funding from the European Union's Horizon 2020 research and innovation programme under the Marie Sklodowska-Curie Grant No. 798556.

[1] J. D. Joannopoulos, S. G. Johnson, J. N. Winn, and R. D. Meade, *Photonic Crystals: Molding the Flow of Light*, 2nd ed. (Princeton University Press, Princeton, 2008).

[2] A. H. Gnauck, R. W. Tkach, A. R. Chraplyvy, and T. Li, High-Capacity Optical Transmission Systems, J. Lightwave Technol. **26**, 1032 (2008).

[3] R. Marqués, F. Martín, and M. Sorolla, *Metamaterials with Negative Parameters: Theory, Design, and Microwave Applications* (2007).

[4] N. Engheta and R. W. Ziolkowski, *Metamaterials: Physics and Engineering Explorations* (John Wiley & Sons, Inc., Hoboken, NJ, USA, 2006).

[5] N. Kaina, F. Lemoult, M. Fink, and G. Lerosey, Ultra small mode volume defect cavities in spatially ordered and disordered metamaterials, Appl. Phys. Lett. **102**, 144104 (2013).

[6] F. Lemoult, N. Kaina, M. Fink, and G. Lerosey, Wave propagation control at the deep subwavelength scale in metamaterials, Nat. Phys. **9**, 55 (2013).

[7] N. Kaina, A. Causier, Y. Bourlier, M. Fink, T. Berthelot, and G. Lerosey, Slow waves in locally resonant metamaterials line defect waveguides, Sci. Rep. **7**, 15105 (2017).

[8] Y. Achaoui, A. Khelif, S. Benchabane, L. Robert, and V. Laude, Experimental observation of locally-resonant and Bragg band gaps for surface guided waves in a phononic crystal of pillars, Phys. Rev. B **83**, 1 (2011).

[9] N. Kaina, F. Lemoult, M. Fink, and G. Lerosey, Negative refractive index and acoustic superlens from multiple

scattering in single negative metamaterials, Nature **525**, 77 (2015).
[10] E. Yablonovitch, Inhibited Spontaneous Emission in Solid-State Physics and Electronics, Phys. Rev. Lett. **58**, 2059 (1987).
[11] L. O'Faolain, T. P. White, D. O'Brien, X. Yuan, M. D. Settle, and T. F. Krauss, Dependence of extrinsic loss on group velocity in photonic crystal waveguides, Opt. Express **15**, 13129 (2007).
[12] S. Mookherjea, J. S. Park, S.-H. Yang, and P. R. Bandaru, Localization in silicon nanophotonic slow-light waveguides, Nat. Photonics **2**, 90 (2008).
[13] A. Yariv, Y. Xu, R. K. Lee, and A. Scherer, Coupled resonator optical waveguide: A proposal and analysis, Opt. Lett. **24**, 711 (1999).
[14] F. Morichetti, C. Ferrari, A. Canciamilla, and A. Melloni, The first decade of coupled resonator optical waveguides: Bringing slow light to applications, Laser Photonics Rev. **6**, 74 (2012).
[15] S. Raghu and F. D. M. Haldane, Analogs of quantum-Hall-effect edge states in photonic crystals, Phys. Rev. A **78**, 1 (2008).
[16] Z. Wang, Y. Chong, J. D. Joannopoulos, and M. Soljacić, Observation of unidirectional backscattering-immune topological electromagnetic states, Nature **461**, 772 (2009).
[17] M. Hafezi, E. A. Demler, M. D. Lukin, and J. M. Taylor, Robust optical delay lines with topological protection, Nat. Phys. **7**, 907 (2011).
[18] K. Fang, Z. Yu, and S. Fan, Realizing effective magnetic field for photons by controlling the phase of dynamic modulation, Nat. Photonics **6**, 782 (2012).
[19] A. B. Khanikaev, S. H. Mousavi, W.-K. Tse, M. Kargarian, A. H. MacDonald, and G. Shvets, Photonic topological insulators, Nat. Mater. **12**, 233 (2013).
[20] W.-J. Chen, S.-J. Jiang, X.-D. Chen, B. Zhu, L. Zhou, J.-W. Dong, and C. T. Chan, Experimental realization of photonic topological insulator in a uniaxial metacrystal waveguide, Nat. Commun. **5**, 5782 (2014).
[21] X. Cheng, C. Jouvaud, X. Ni, S. H. Mousavi, A. Z. Genack, and A. B. Khanikaev, Robust reconfigurable electromagnetic pathways within a photonic topological insulator, Nat. Mater. **15**, 542 (2016).
[22] Y. G. Peng, C. Z. Qin, D. G. Zhao, Y. X. Shen, X. Y. Xu, M. Bao, H. Jia, and X. F. Zhu, Experimental demonstration of anomalous Floquet topological insulator for sound, Nat. Commun. **7**, 13368 (2016).
[23] L.-H. Wu and X. Hu, Scheme for Achieving a Topological Photonic Crystal by Using Dielectric Material, Phys. Rev. Lett. **114**, 223901 (2015).
[24] T. Ma and G. Shvets, All-Si valley-Hall photonic topological insulator, New J. Phys. **18**, 025012 (2016).
[25] S. Yves, R. Fleury, T. Berthelot, M. Fink, F. Lemoult, and G. Lerosey, Crystalline metamaterials for topological properties at subwavelength scales, Nat. Commun. **8**, 16023 (2017).
[26] M. Goryachev and M. E. Tobar, Reconfigurable Microwave Photonic Topological Insulator, Phys. Rev. Appl. **6**, 1 (2016).
[27] J. E. Vázquez-Lozano and A. Martínez, Optical Chirality in Dispersive and Lossy Media, Phys. Rev. Lett. **121**, 43901 (2018).
[28] F. Alpeggiani, K. Y. Bliokh, F. Nori, and L. Kuipers, Electromagnetic Helicity in Complex Media, Phys. Rev. Lett. **120**, 243605 (2018).
[29] S. Papantonis, S. Lucyszyn, and E. Shamonina, Dispersion effects in Fakir's bed of nails metamaterial waveguides, J. Appl. Phys. **115**, 054903 (2014).
[30] G. W. Mulholland, C. F. Bohren, and K. a Fuller, Light scattering by agglomerates: Coupled electric and magnetic dipole method, Langmuir **10**, 2533 (1994).
[31] See Supplemental Material at http://link.aps.org/supplemental/10.1103/PhysRevApplied.10.054069 for the details of semi-analytical model, band structures of chiral metamolecule and interface, fabrication of samples and experimental setup, the different schemes of waveguiding and details of statistical analysis.
[32] P. W. Anderson, Absence of diffusion in certain random lattices, Phys. Rev. **109**, 1492 (1958).
[33] N. F. Mott, Electrons in disordered structures, Adv. Phys. **16**, 49 (1967).
[34] T. Kariyado and X. Hu, Topological states characterized by mirror winding numbers in graphene with bond modulation, Sci. Rep. **7**, 1 (2017).